Strain in buried self-assembled SiGe wires studied by grazing-incidence x-ray diffraction

T. Roch, V. Holý,* A. Hesse, J. Stangl, T. Fromherz, and G. Bauer
Institut für Halbleiterphysik, Johannes Kepler Universität, A-4040 Linz, Austria

T. H. Metzger and S. Ferrer
European Synchrotron Radiation Facility, F-38042 Grenoble Cedex 9, France

(Received 11 December 2001; revised manuscript received 21 March 2002; published 24 June 2002)

For the calculation of strain fields of buried self-assembled SiGe wires in a SiGe/Si multilayer, an analytical model has been developed. It is applied for a simulation of the diffraction pattern from buried wires, which were investigated by grazing-incidence x-ray diffraction. The simulations are based on the distorted-wave Born approximation, and using the analytical approach for calculating the inhomogeneous elastic strain fields within the wires and in the surrounding Si matrix, computation times can be considerably decreased. In the measured reciprocal space maps, satellite intensity maxima indicate a good lateral and vertical correlation of the wire positions. Both from the grazing-incidence diffraction and from photoluminescence, an average Ge content in the wires of 20% is found, considerably *lower* than the deposited value of 45%. The resulting lateral maximum elastic relaxation of the wire lattice is about 85% on the top ridge.

DOI: 10.1103/PhysRevB.65.245324 PACS number(s): 61.10.Dp, 68.65.−k, 68.65.La

I. INTRODUCTION

Self-organized semiconductor nanostructures have attracted a lot of interest in recent years, because they offer vast opportunities for fundamental studies of the epitaxial growth as well as because of their potential for semiconductor devices. Since their size, shape, composition, and strain status influence their electronic and optical properties, a lot of effort has been devoted in the past to their structural analysis. In the self-organization process, growth instabilities, either of kinetic nature or strain-induced ones,[1] are exploited for fabrication of semiconductor nanostructures. The nucleation of islands on wetting layers (WL's) via the Stranski-Krastanow mechanism has been studied intensively for the heteroepitaxy of sufficiently strained systems.[2] The surface morphology of such islands has been investigated by atomic force microscopy[3] (AFM) and scanning tunneling microscopy (STM),[4] buried islands were studied by transmission electron microscopy[5,6] (TEM) and cross-sectional STM.[7] Furthermore, high-angle x-ray diffraction,[8] as well as surface sensitive grazing-incidence diffraction[9] (GID) and grazing incidence small-angle x-ray scattering[10] (GISAXS) techniques were employed to study the strain status, the size, and the shape of the islands.

Whereas self-assembled islands were studied extensively so far, much less work was devoted to self-assembled quantum wires. They can serve as templates for the growth of quantum dots, and due to their homogeneity in one direction offer an easier research approach narrowed on the cross-section plane properties. Several different approaches have been used to achieve self-assembled wire growth.

(i) Tersoff and Tromp[11] have shown that strained epitaxial layers, which tend initially to grow as dislocation-free islands, may exhibit a shape transition to elongated islands and herewith allow better stress relaxation. This eventually can lead to self-organized wires on nominally flat substrates. The mechanism was demonstrated recently for the growth of InGaAs/GaAs multilayer structures deposited on (001) GaAs with a miscut smaller than 0.05°.[12]

(ii) Selective growth on prepatterned substrates can result in quantum wires.[13]

(iii) It was shown that the *step bunching* process in SiGe/Si multilayers grown on vicinal Si (001) and (113) substrates can lead to more or less regularly arranged terraces, which serve as suitable templates for the subsequent formation of Ge rich wires or islands.[14,15]

So far, the main mechanism leading to island or wire growth was attributed to a thermodynamically driven growth instability, associated with the partial relaxation of strain at the surface steps, and strain relaxation of the islands and the wires.[16] More recent investigations point to the important influence of kinetic growth instabilities for the growth of Si as well as of SiGe on vicinal (001) Si substrates.[17,18] Strained SiGe material epitaxially deposited on such stepped surfaces may form wirelike stripes. Whether elongated islands or wires are formed on such terraces, depends critically on the growth conditions.[14,19,20]

X-ray scattering methods have a large potential for the shape and strain analysis of semiconductor heterostructures and embedded nanostructures.[21] The scanning microscopy techniques (such as AFM, TEM, Scanning electron microscopy) have high spatial resolution, but they are often destructive and have a rather small investigated sample area (μm^2,nm^2). In contrast, the nondestructive x-ray techniques have high resolution in reciprocal space and the measured data provide statistical information from sample areas of the order of several mm^2. Especially x-ray diffraction techniques are very suitable for the determination of the strain status of buried and also free-standing nanostructures.[9,22,23] Grazing-incidence setups allow for certain depth resolution and better intensity contrast due to the decrease of scattering from the substrate. However, the data analysis of strain fields is so far based on fitting procedures using model calculations, and especially the calculation of strain using the finite element method (FEM) is very time consuming.

We have developed an alternative analytical method to

 ©2002 The American Physical Society

calculate the strain distribution in buried nanostructures, which is faster and also easier to implement into, e.g., x-ray scattering simulations. For a first application of the method, we investigate a SiGe wire sample, where modeling needs to be performed in two dimensions only. There is, however, no general restriction of the method to two-dimensional models. We choose a SiGe wire sample for this study, because the sample structure and wire shape are already known from previous GISAXS measurements.[24] Here, we obtain additional information on the Ge content, and on the elastic relaxations within the SiGe wires and in the surrounding Si matrix.

In contrast to earlier work, our method takes the elastic relaxation at the sample surface into account, which is important for structures close to the surface. The results of our analytical calculations are compared to conventional FEM calculations, and found to obtain nearly identical results. The calculated displacement fields are used as an input for simulations of the scattered intensity in strain sensitive GID geometry, based on distorted-wave Born approximation.

The paper is organized as follows: In Sec. II experimental data are presented. Section III deals with the calculation of the displacement fields induced by a stack of buried self-assembled SiGe wires, and describes the calculation of the scattered x-ray intensities in GID geometry. In Sec. IV the analysis of the scattering data is presented, and the results are compared to an analysis of photoluminescence spectra. Finally the results are summarized in Sec. V.

II. EXPERIMENTS

In this work we have investigated a series of samples containing SiGe quantum wires grown in a self-organized regime by solid source molecular-beam epitaxy (MBE). The samples consist of 20 periods of nominally 25-Å-thick $Si_{1-x}Ge_x$ layers separated by 100-Å Si layers. The nominal Ge content x of the alloy layers is 0.35, 0.40, and 0.45 for samples *A*, *B*, and *C*, respectively. In order to initiate step bunching and the wire growth, a vicinal (001) Si substrate with a rather large miscut angle $\beta = 3.5°$ towards the [100] direction was chosen. All samples were capped with a 100-Å-thick Si layer. The details on the MBE growth are described in Ref. 25.

Figure 1 shows an atomic force micrograph of sample *C*, which exhibits a pronounced one-dimensional periodic ripple structure at the Si surface, with the ripples oriented perpendicular to the substrate miscut, i.e., along the [010] direction. Since the height of these surface ripples is rather low (with a peak-to-valley height difference of about 6 Å), this surface corrugation does not contribute significantly to the scattered x-ray intensity. The inset shows the autocorrelation function, demonstrating that a correlation of the wire positions extends over about six mean ripple periods; this period is about 890 Å.

Whereas with AFM only the surface of the Si cap layer can be investigated, x-ray diffraction and small-angle scattering experiments can yield information on the buried structures as well. Scattering experiments were performed in coplanar high-resolution x-ray diffraction (HRXRD) geometry,

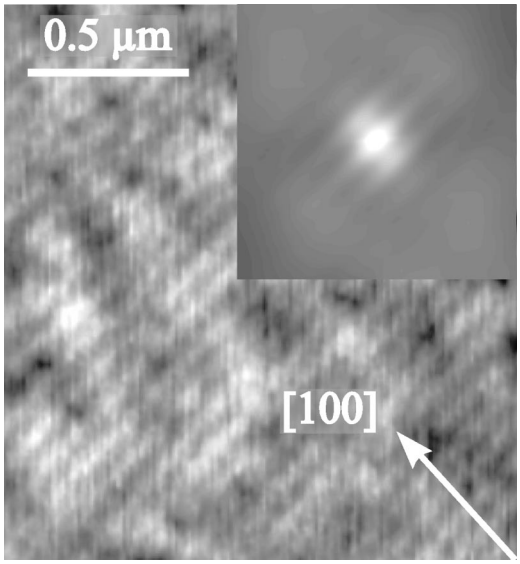

FIG. 1. AFM image of the top Si surface of the investigated Si/SiGe multilayer sample *C*. The inset shows the autocorrelation function of the surface calculated from the AFM data.

as well as in GID and GISAXS geometries. In HRXRD and GID we have detected the scattered intensity as a function of the reduced scattering vector $\mathbf{Q} = \mathbf{K}_f - \mathbf{K}_i - \mathbf{h}$, where $\mathbf{h}$ is the diffraction vector (i.e., the vector of the reciprocal lattice) and $\mathbf{K}_{i,f}$ are the wave vectors of the primary and scattered beams.

GISAXS experiments have been carried out in order to get information on the shape of the buried wires, the results can be found in Ref. 24. The GISAXS spectra clearly showed that the buried SiGe wires have a triangular cross section with a base length of about 350 Å, and a slope (facet) angle of about 6°, i.e., *larger* than the miscut angle $\beta = 3.5°$. The lengths of the SiGe wires are about 2500 ± 500 Å, actually similar to the feature lengths on the sample surface, as determined by AFM.

We have performed an HRXRD Q_z scan around the symmetrical (004) reciprocal lattice point using a laboratory x-ray source with Cu $K\alpha_1$ radiation, a four-crystal Ge(220) Bartels monochromator, and an open detector. Figure 2 shows the measured data (dots) together with the integrated intensities (open circles) of the superlattice (SL) peaks and a simulation based on dynamical scattering theory (solid line). From the peak distance an SL period of 128 ± 1 Å follows. Due to the buried wire structure and the limited detector resolution, the peaks are broadened, therefore we have fitted the envelope curve of *integrated intensities* of the broadened peaks, instead of the peak values of the intensity satellites. In the simulation we assumed a layered structure, where the SiGe layer was divided into the WL and an effective wire layer. The latter is a layer with a thickness equal to the wire height as obtained from GISAXS data and a Ge content corresponding to the lateral average over the wires and the surrounding Si matrix. However, an unambiguous fit of all the parameters of both layers is not possible. For instance, if we assume a Ge content of $x = 20\%$ in the wires, we obtain for the Ge concentration and for the thickness of the WL the

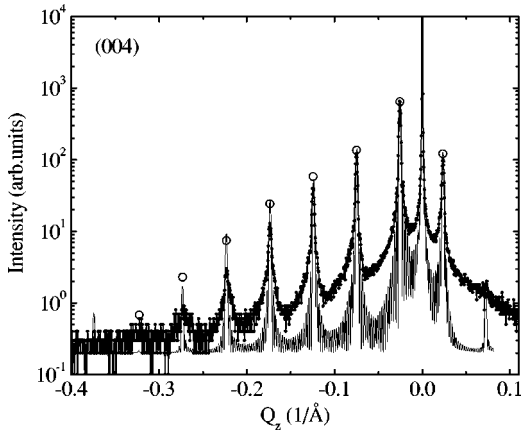

FIG. 2. Q_z scan of sample *C* around the (004) reciprocal lattice point (points), with the integrated intensities of the peaks (circles), together with the simulation (line).

values 32% and 28 Å, respectively. For another choice of $x = 30\%$ in the wire, for the WL the values 33% and 25 Å follow.

In HRXRD, the intensity distribution is strongly influenced by the in-plane and vertical components of the strain fields in the wires and the surrounding Si matrix. In order to enhance the sensitivity for the in-plane strain component, as well as the sensitivity to the rather thin wire stack, we employed GID geometry. For an orientation of the wires along the [010] direction, the (400) and (040) reciprocal lattice points are suitable, with the diffraction vector perpendicular and parallel to the wires, respectively. The diffracting crystal lattice planes are perpendicular to the sample surface, so that the diffraction plane lies in the Q_xQ_y plane as sketched in Fig. 3(a). By simultaneous movement of the sample and detector (i.e., by changing the directions of the wave vectors $\mathbf{K}_i$ and $\mathbf{K}_f$) we perform a so-called *longitudinal* scan, whereas a *transversal* scan is recorded by moving solely the sample azimuthal position.

Figure 3(b) outlines the relation between the orientations of the wires in real space and the Q_x and Q_y coordinates in reciprocal space. The intensity satellites due to wires are sketched schematically. In the transversal geometry, the length of the scattering vector $\mathbf{Q} \approx \mathbf{h}$ is approximately constant throughout the map and perpendicular to the displacements, hence this geometry is not strain sensitive. In the longitudinal setup the diffraction vector is parallel to the in-plane displacements, hence this geometry gives a good strain sensitivity.

The shape of the wires, which enters the numerical calculations of the diffracted intensity described below, is sketched in Fig. 3(c). We use the triangular wire cross section obtained from previous GISAXS measurements,[24] which is determined by three parameters: the width of the wire base *A*, and two angles $\beta_{1,2}$ of the side facets. The direction of the correlation of the wire *positions* at different interfaces is not always vertical but can also be inclined by angle χ with respect to the growth direction.[28] For such an arrangement we will use in the following the expression *oblique replication*.

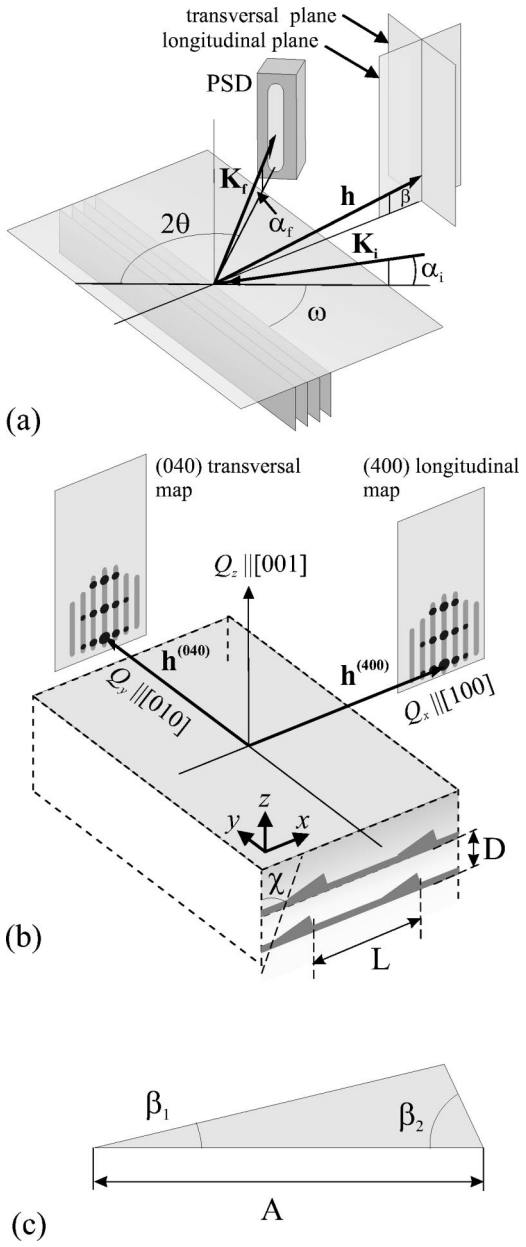

FIG. 3. (a) Sketch of the GID geometry: $\mathbf{K}_i$ and $\mathbf{K}_h$ are the wave vectors of the primary and scattered beams, respectively, $\mathbf{h}$ is the diffraction vector, $\alpha_{i,f}$ denote the angles of incidence and exit, respectively. (b) Definition of the coordinate system in reciprocal space and the geometries for the reciprocal space maps denoted ''longitudinal'' and ''transversal.'' (c) Sketch of the wire cross section assumed in the calculations.

The GID experiments were carried out at the TROÏKA and ID3 beamlines at the ESRF, Grenoble, using a wavelength of $\lambda = 1.55$ Å, a diamond (111) double crystal monochromator (TROÏKA) or a Si (111) double monochromator (ID3). The scattered intensity was recorded using a linear position sensitive detector placed at a distance of 900 mm from the sample. Its orientation was perpendicular to the sample surface, so that a detector line spectrum corresponds roughly to the Q_z direction. The scattered radiation is analyzed spatially as a function of the exit angle α_f by 1024

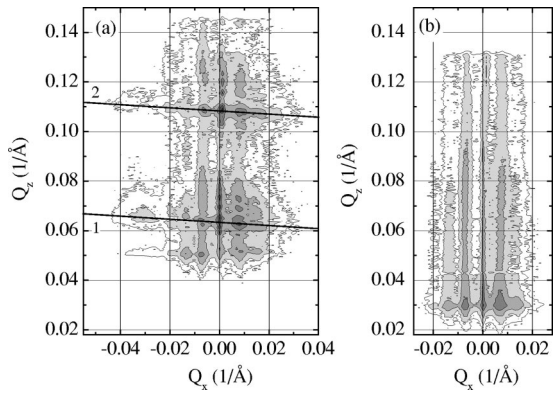

FIG. 4. Longitudinal (400) reciprocal space maps measured with incidence angles $\alpha_i = 0.5°$ (a) and $\alpha_i = 0.2°$ (b). The step of the contour lines is $10^{0.25}$. In panel (a) the lines denoted 1 and 2 correspond to the trajectories of extracted line scans shown in Fig. 8.

detector channels. Hence, two-dimensional reciprocal space maps were recorded in single scans. The resolution in reciprocal space was $\Delta Q_z = 5 \times 10^{-4}$ Å^{-1}, $\Delta Q_x = 3.7 \times 10^{-3}$ Å^{-1}, and $\Delta Q_x = 2.6 \times 10^{-3}$ Å^{-1} for the maps in (400) and (040) diffractions, respectively.

The (400) maps denoted as ''longitudinal'' are plotted for two different angles of incidence $\alpha_i = 0.5°$ and $\alpha_i = 0.2°$ in Figs. 4(a) and 4(b), respectively. For $\alpha_i = 0.5°$ the angle of incidence is above the critical angle of total external reflection and hence the x rays penetrate through the whole SL stack. Thus we observe several intensity maxima along Q_z reflecting the periodic structure along the [001] direction. The lateral intensity satellites reflect the lateral periodicity of the wires.

The lines denoted by 1 and 2 drawn through the lateral intensity maxima in Fig. 4(a) are slightly inclined by an angle χ with respect to the horizontal Q_x axis. This indicates that the wire positions at different SiGe/Si interfaces are replicated obliquely along a direction inclined by an angle χ.

For $\alpha_i = 0.2°$, as shown in Fig. 4(b), no periodic intensity extrema along the Q_z direction occur, as for incidence angles below the critical angle the penetration depth of x rays is very small and only the top layer of wires contributes to the scattered intensity. In this figure, the intensity maxima observable on the vertical rods for the smallest Q_z do not stem from the vertical correlation of the wire positions, they are caused by the maxima of the factor $|t_i t_f|^2$ in Eq. (25). These maxima occur if α_i and/or α_f (angle of exit of the scattered beam) equal α_c.[29]

As a cross check of the GID measurements, low-temperature (T = 4.2 K) photoluminescence (PL) has been measured. The spectra of samples *A*, *B*, and *C* are shown in Fig. 5. The PL was excited by the 514-nm line of an Ar^+ laser with an intensity of 160 mW. The spectrum of the sample with the lowest Ge content (sample *A*) is typical for a two-dimensional SiGe quantum well layer: The lines at 0.997 eV, 0.979 eV, and at 0.940 eV (labeled NP_{WL}, TA_{WL}, and TO_{WL} in Fig. 5) are commonly attributed to the no-phonon (NP) luminescence of a SiGe quantum well exciton and its transverse-acoustic and transverse-optical phonon replicas.[26,27] No indication of PL from quantum wires is observed in the spectrum of sample *A*. Therefore, we conclude that in this sample no quantum wires have formed, which is also found in HRXRD measurements of the sample. The PL spectra of samples *B* and *C* with higher Ge contents are significantly different: In addition to the strongly quenched NP_{WL} line and its phonon replica, additional PL peaks appear in the spectra: a broad PL line (labeled NP_{WR}) is observed ≈ 20 meV below the NP_{WL} line. This peak dominates any contribution of the TA_{WL} line possibly present in the spectra of samples *B* and *C*. We assign the NP_{WR} peak to PL from excitons confined to the self-organized quantum wires. For sample *C* with the highest Ge content, the NP_{WR} becomes the strongest signal in the PL spectrum. In addition to the NP_{WR} peak, also the TO replica (TO_{WR}) is clearly resolved in the spectrum of sample *C*. For sample *B*, the TO_{WR} signal is less pronounced and appears as a shoulder in the PL spectrum. Since the signature of the quantum wire PL is strongest for sample *C*, the experiments aiming at the structural characterization of the self-assembled quantum wires concentrate on this sample.

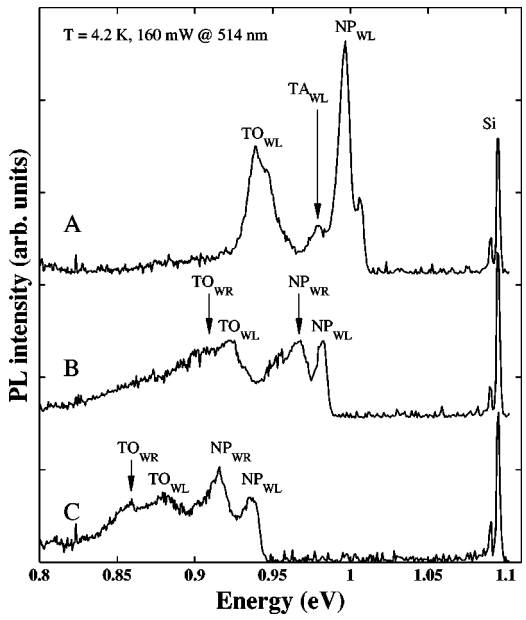

FIG. 5. Low-temperature photoluminescence (PL) spectra of samples *A*, *B*, and *C*. The nominal composition of the three samples is given in the text. Besides the PL from the Si substrate and the Si epilayers around 1.09 eV, strong PL signals from the SiGe alloy layers are observed for energies below 1 eV. For sample *A* with the lowest Ge content (nominal 35%), a PL spectrum characteristic for a SiGe quantum well is observed. In addition to the wetting layer luminescence, PL lines ascribed to the recombination of excitons in the quantum wire appear in the spectra of the samples with higher nominal Ge content (sample *B*, 40%; *C*, 45%). The PL peaks are labeled according to the type of phonons involved in the exciton recombination (NP, no phonon; TO, transverse optic; TA, transverse acoustic) with a subscript indicating the sample region in which the recombination occurs (WL, wetting layer; WR, quantum wire)

III. THEORY

For the simulation of the GID measurements it is necessary to calculate the elastic deformation of the crystal lattice

in the wires and around them. This is described below in part A, followed by the calculation of the scattered intensity in part B.

A. Displacement field of a periodic array of buried quantum wires

The most frequently applied method for the calculation of the strain distribution in and around nanostructures is the FEM. However, the disadvantage of FEM is that it is rather time consuming, and any change of, e.g., a wire shape requires a change of the calculation grid, so that FEM cannot be easily included into a software simulating and fitting x-ray scattering patterns. Therefore, we have developed an analytical approach for the calculation of the displacement field of wires buried below the sample surface. Recently, a similar analytic method for the calculation of the strains around a periodic sequence of etched quantum wires has been developed,[30] which is valid in the limit of elastic isotropy.

We start from the equilibrium equations[31]

$$\frac{\partial \sigma_{jk}}{\partial x_k} + f_j = 0, \quad j,k = x,y,z, \tag{1}$$

where

$$\sigma_{jk} = C_{jklm}\varepsilon_{lm} \tag{2}$$

are the components of the stress tensor, ε_{lm} are the components of the strain tensor, C_{jklm} are the elastic constants of the material, and f_j are the components of the volume force density caused by the lattice mismatch of the wire lattice with respect to the host crystal. At the free sample surface the boundary conditions

$$\sigma_{jk} n_k|_{\text{surface}} = 0, \ \ j = x,y,z \tag{3}$$

have to be fulfilled, where **n** is the vector of the surface normal.

In order to be able to solve the problem analytically, we perform the following simplifications.

(1) We restrict ourselves to a cubic crystal with a (001) surface and the wires along [010]. Then, the material is described by three elastic constants; in the well-known 6×6 $C_{\alpha\beta}$ notation,[31] the independent constants are C_{11}, C_{12}, and C_{44}. In fact, this simplification is not crucial for the possibility of an analytic solution of Eq. (1), but it simplifies the formulas substantially.

(2) We assume that the sample surface is ideally flat. This assumption simplifies the form of the boundary conditions (2) and it is necessary for an analytic calculation. Therefore, the calculation method is suitable only for wires buried below a free surface.

(3) Strictly speaking, Eq. (1) is valid only if the elastic constants are the same everywhere in the sample volume. Therefore, we have to neglect the difference between the elastic constants of the Si matrix and of the wire SiGe lattice. However, the elastic constants of the wires affect substantially the volume force density. Therefore, we assume the validity of Eq. (1), but in the expression for the force density we include the elastic constants $C^{\text{w}}_{\alpha\beta}$ of the wire lattice depending on its chemical composition. As we show later, the results of this approximative approach compare well with exact simulations based on FEM. The volume force density is then given by[31]

$$f_j = -F\frac{\partial \Omega(\mathbf{r})}{\partial x_j}, \quad F = (C^{\text{w}}_{11} + 2C^{\text{w}}_{12})\,\delta, \tag{4}$$

where $\Omega(\mathbf{r})$ is the shape function of the wire array (unity in the SiGe wires and zero outside them) and $\delta = (a_{\text{w}} - a_{\text{Si}})/a_{\text{Si}}$ is the relative mismatch of the wire lattice with respect to the host lattice.

For the calculation of the displacement field of a wire structure we define the coordinate system according to Fig. 3. The free surface is at $z = T$, and the wires are elongated parallel to the y axis [010]. We assume that the wires are infinitely long and homogeneous along y, therefore both the force density and the displacement field $\mathbf{u}(\mathbf{r})$ depend only on x and z. In addition, for the wires parallel to [010] and for cubic symmetry of $C_{\alpha\beta}$ the displacement vector $\mathbf{u}(\mathbf{r})$ is always perpendicular to the wires, i.e., $u_y = 0$. For wire orientations with lower symmetry, however, $u_y \neq 0$ may occur.

For the Fourier component of the displacement field

$$\mathbf{u}^{\text{F}}(k,z) \equiv \begin{pmatrix} u^{\text{F}}_x(k,z) \\ u^{\text{F}}_z(k,z) \end{pmatrix} = \int_{-\infty}^{\infty} dx\, \mathbf{u}(x,z) e^{-ikx}, \tag{5}$$

we obtain from Eq. (1) the matrix equation

$$\hat{\mathbf{A}}(\mathbf{u}^{\text{F}})'' + i\hat{\mathbf{B}}(\mathbf{u}^{\text{F}})' - \hat{\mathbf{C}}\mathbf{u}^{\text{F}} = \mathbf{P}, \tag{6}$$

where

$$\hat{\mathbf{A}}(k) = \begin{pmatrix} C_{44} & 0 \\ 0 & C_{11} \end{pmatrix},$$

$$\hat{\mathbf{B}}(k) = \begin{pmatrix} 0 & k(C_{12}+C_{44}) \\ k(C_{12}+C_{44}) & 0 \end{pmatrix},$$

$$\hat{\mathbf{C}}(k) = \begin{pmatrix} k^2 C_{11} & 0 \\ 0 & k^2 C_{44} \end{pmatrix} \tag{7}$$

and the vector on the right-hand side of Eq. (6) is

$$\mathbf{P}(k,z) = F\begin{pmatrix} ik\Omega^{\text{F}} \\ (\Omega^{\text{F}})' \end{pmatrix}. \tag{8}$$

We have denoted the derivative with respect to z by a prime ($'$). $\Omega^{\text{F}}(k,z)$ is the one-dimensional Fourier transformation of $\Omega(x,z)$.

The boundary conditions for $\mathbf{u}^{\text{F}}$ at the free surface and at the rear sample surface far below the wire array are

$$\hat{\mathbf{A}}(\mathbf{u}^{\text{F}})' + i\hat{\mathbf{D}}\cdot\mathbf{u}^{\text{F}}|_{z=T, z\to-\infty} = 0, \tag{9}$$

where

$$\hat{\mathbf{D}}(k) = \begin{pmatrix} 0 & kC_{44} \\ kC_{12} & 0 \end{pmatrix}. \tag{10}$$

The general solution of Eq. (6) is a sum of a general solution $\mathbf{v}_g$ of a homogeneous equation

$$\hat{\mathbf{A}}(\mathbf{v}_g)'' + i\hat{\mathbf{B}}(\mathbf{v}_g)' - \hat{\mathbf{C}}\mathbf{v}_g = 0 \tag{11}$$

and any particular solution $\mathbf{v}_p$ of the full Eq. (6). The general solution of the homogeneous equation is a linear combination of the eigensolutions

$$\mathbf{v}_g(k,z) = \sum_{n=1}^{4} c_n(k)\mathbf{v}_n(k)e^{i\kappa_n(k)z}, \tag{12}$$

where $\kappa_{1,\ldots,4}$ are the roots of the characteristic equation

$$\det[\hat{\mathbf{W}}(k,\kappa)] \equiv \det(\hat{\mathbf{A}}\kappa^2 + \hat{\mathbf{B}}\kappa + \hat{\mathbf{C}}) = 0 \tag{13}$$

and $\mathbf{v}_n$ are the corresponding eigenvectors

$$\hat{\mathbf{W}}(k,\kappa_n)\mathbf{v}_n = 0. \tag{14}$$

The particular solution of the full equation can be expressed using the two-dimensional Fourier transformation

$$\mathbf{v}_p^{\mathrm{FF}}(k,q) = \int_{-\infty}^{\infty} dz \mathbf{v}_p(k,z)e^{-iqz}$$

of the displacement field as

$$\mathbf{v}_p^{\mathrm{FF}}(k,q) = -[\hat{\mathbf{W}}(k,q)]^{-1}\mathbf{P}^{\mathrm{FF}}(k,q). \tag{15}$$

The inverse Fourier transform can be performed using the residuum theorem. κ_{n+} and κ_{n-} denote the eigenvalues with positive and negative imaginary parts, respectively, and we obtain the final expression for the displacement field

$$\begin{aligned}\mathbf{u}^{\mathrm{F}}(k,z) = &\sum_{n=1,\ldots,4} c_n\mathbf{v}_n e^{i\kappa_n z} \\ &+ \frac{F}{C_{11}C_{44}}\left[\sum_{n+} \Omega^{+}(k,\kappa_{n+},z)\mathbf{w}_{n+}e^{iz\kappa_{n+}}\right. \\ &\left. - \sum_{n-} \Omega^{-}(k,\kappa_{n-},z)\mathbf{w}_{n-}e^{iz\kappa_{n-}}\right],\end{aligned} \tag{16}$$

where

$$\mathbf{w}_n = \frac{1}{\Pi_{j\neq n}(\kappa_n - \kappa_j)}\begin{pmatrix} C_{44}k(k^2-\kappa_n^2) + (C_{11}-C_{12})k\kappa_n^2 \\ C_{44}\kappa_n(\kappa_n^2 - k^2) + (C_{11}-C_{12})k^2\kappa_n \end{pmatrix}$$

and

$$\begin{aligned}\Omega^{+}(k,\kappa,z) &= \int_{-\infty}^{\infty} dx' \int_{-\infty}^{z} dz' \Omega(x',z')e^{-i(kx'+\kappa z')}, \\ \Omega^{-}(k,\kappa,z) &= \int_{-\infty}^{\infty} dx' \int_{z}^{T} dz' \Omega(x',z')e^{-i(kx'+\kappa z')}.\end{aligned} \tag{17}$$

The coefficients c_n in Eq. (16) can be determined from the boundary conditions (9). From the boundary condition at the rear surface ($z\to-\infty$) $c_{n+}=0$ follows. The remaining two coefficients c_{n-} are obtained from the boundary conditions at $z=T$ that can be written in the form

$$\begin{aligned}\sum_{n-} c_{n-}(\kappa_{n-}v_{xn-} + kv_{zn-})e^{iT\kappa_{n-}} &= -\frac{F}{C_{11}C_{44}}\sum_{n+}(w_{xn+}\kappa_{n+} + w_{zn+}k) \\ &\quad\times\Omega^{\mathrm{FF}}(k,\kappa_{n+})e^{iT\kappa_{n+}},\end{aligned} \tag{18}$$

$$\begin{aligned}\sum_{n-} c_{n-}(C_{11}\kappa_{n-}v_{zn-} + C_{12}kv_{xn-})e^{iT\kappa_{n-}} &= -\frac{F}{C_{11}C_{44}}\sum_{n+}(C_{11}w_{zn+}\kappa_{n+} \\ &\quad + C_{12}w_{xn+}k)\Omega^{\mathrm{FF}}(k,\kappa_{n+})e^{iT\kappa_{n+}},\end{aligned} \tag{19}$$

where

$$\begin{aligned}\Omega^{\mathrm{FF}}(k,\kappa) &= \int_{-\infty}^{\infty} dz\Omega^{\mathrm{F}}(k,z)e^{-i\kappa z} \\ &= \int_{-\infty}^{\infty} dx \int_{-\infty}^{\infty} dz\Omega(x,z)e^{-i(kx+\kappa z)}\end{aligned}$$

is the two-dimensional Fourier transformation of the shape function of the wire array.

We assume that the individual wires in the multilayer have identical shapes $\Omega_{\mathrm{w}}(x,z)$ and they are perfectly periodically distributed at the SiGe-Si interfaces with the lateral period L and the (vertical) period of the multilayer D (see Fig. 3). We assume also a perfect oblique replication of the wire positions determined by a given angle χ. Then the shape function of the wire array can be expressed as

$$\Omega(x,z) = \sum_{m_x=-\infty}^{\infty}\sum_{m_z=0}^{N-1}\Omega_{\mathrm{w}}(x - m_xL - m_zD\tan[\chi], z - m_zD),$$

where N is the number of (vertical) periods in the multilayer. This yields

$$\begin{aligned}\Omega^{+-}(k,\kappa,z) = \frac{2\pi}{L}\sum_{P}\delta(k-P)\sum_{m_z=0}^{N-1}&\Omega_{\mathrm{w}}^{+-} \\ &\times(P,\kappa,z-m_zD)e^{-im_zD[\kappa + k\tan(\chi)]}\end{aligned}$$

with

$$\begin{aligned}\Omega_{\mathrm{w}}^{+}(k,\kappa,z) &= \int_{-\infty}^{\infty} dx' \int_{-\infty}^{z} dz' \Omega_{\mathrm{w}}(x',z')e^{-i(kx'+\kappa z')}, \\ \Omega_{\mathrm{w}}^{-}(k,\kappa,z) &= \int_{-\infty}^{\infty} dx' \int_{z}^{T} dz' \Omega_{\mathrm{w}}(x',z')e^{-i(kx'+\kappa z')}.\end{aligned}$$

We have denoted by $P = 2\pi p/L$ (p is an integer) the vectors of a one-dimensional lattice reciprocal to the one-dimensional wire array. Since the functions $\Omega^{+-}(k,\kappa,z)$ are

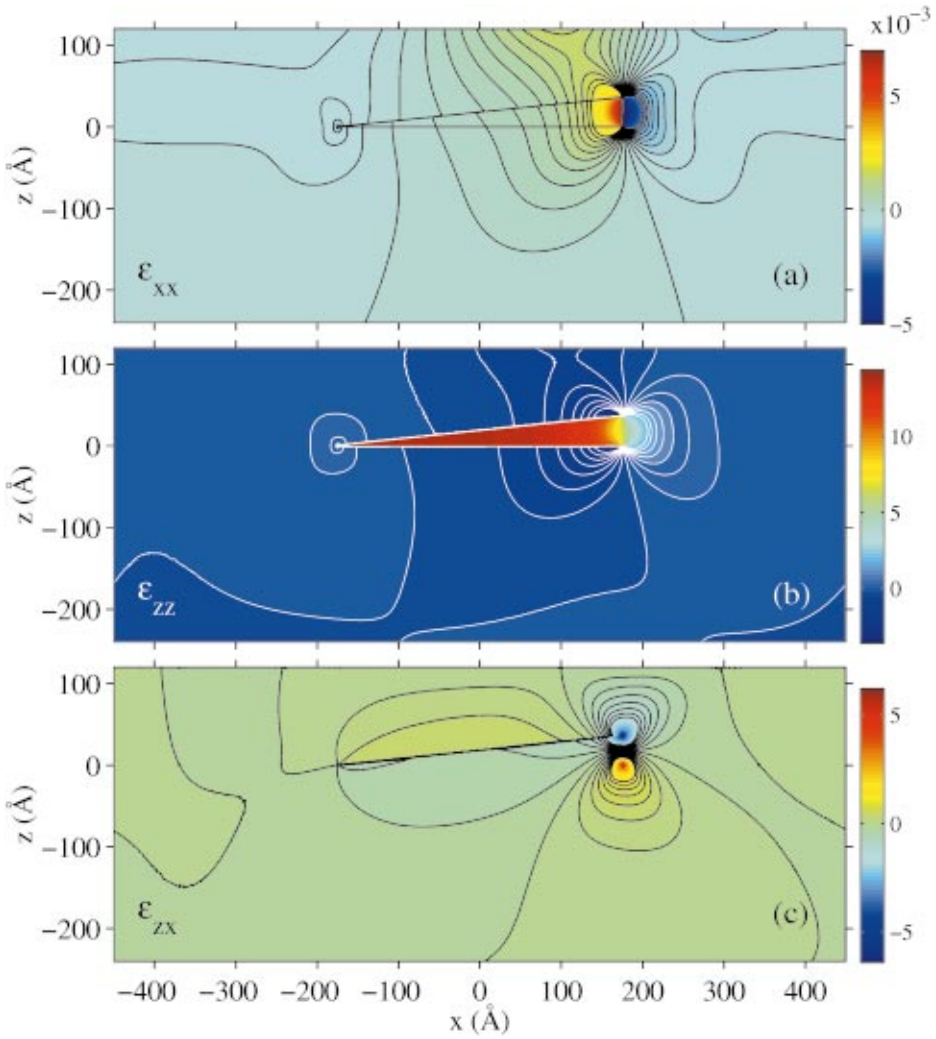

FIG. 6. (Color) Distributions of the strain tensor components ϵ_{xx} (a), ϵ_{zz} (b), and ϵ_{zx} (c) obtained from analytical calculation. The parameters of the wire are $A=350$ Å, $\beta_1=6°$, $\beta_2=90°$, $x_{\mathrm{Ge}}=0.2$, and the depth of the wire base below the surface was 120 Å. The step of the contours is $\Delta\epsilon_{xx}=\Delta\epsilon_{xz}=2\times10^{-4}$, and $\Delta\epsilon_{zz}=3\times10^{-4}$ in the respective panels.

superpositions of δ-like peaks centered in this reciprocal wire lattice, the displacement field has the form of a Fourier series

$$\mathbf{u}(x,z)=\sum_P \mathbf{u}^{\mathrm{F}}(P,z)e^{iPx}, \tag{20}$$

where the coefficients $\mathbf{u}^{\mathrm{F}}(P,z)$ are given by Eq. (16).

In order to demonstrate the applicability of the procedure above, we have simulated the distribution of the strain tensor components

$$\epsilon_{xx}=\frac{\partial u_x}{\partial x}, \quad \epsilon_{zz}=\frac{\partial u_z}{\partial z}, \quad \text{and} \quad \epsilon_{zx}=\frac{1}{2}\left(\frac{\partial u_z}{\partial x}+\frac{\partial u_x}{\partial z}\right)$$

of a single buried wire with a triangular cross section buried 120 Å below the free relaxed surface, the shape of the wire is obtained from GISAXS data (see below). The strain components ϵ_{xx}, ϵ_{zz}, and ϵ_{zx} of the strain calculated with the analytical model for $x_{\mathrm{Ge}}=20\%$ are shown in Figs. 6(a), 6(b), and 6(c), respectively. In order to achieve a sufficient resolution in real space, we have used a large set of the values of P, the difference δP of the neighboring P values in this set was chosen much smaller than $2\pi/\Delta x$, where Δx is the range of the x coordinates in Fig. 6. In this figure, we have also suppressed the overlapping of the deformation fields of neighboring wires by choosing their distance $2\pi/\delta P$ sufficiently large. The influence of the surface stress relaxation [Eq. (3)] on the strain distribution is substantial, if the depth of the wire below the surface does not exceed few thousands of angstroms. Therefore, one can expect that the relaxation affects the scattered intensity mainly for scattering geometries with a small penetration depth of the incident x-ray beam, such as in GID.

The in-plane component ϵ_{xx} exhibits a maximum tensile strain of about 0.7% near the steeper side facet of the triangular wire. This value corresponds to the lateral elastic relaxation of about 85% with respect to fully relaxed bulk $Si_{0.8}Ge_{0.2}$. In the surrounding Si matrix close to this facet of the wire a maximum compressive lateral strain of the order of 0.6% occurs. The distribution of the ϵ_{zz} component is plotted in Fig. 6(b). The maximum value of ϵ_{zz} is about 1.45%, which nearly equals the vertical strain in a pseudomorphic tetragonally distorted homogeneous $Si_{0.8}Ge_{0.2}$ layer. Above and below the wire, the Si lattice is compressed vertically by about 0.3% in maximum.

The validity of our analytical method is demonstrated in Fig. 7, where we compare the x and z components of the displacement vector $\mathbf{u}(x,z)$ calculated using FEM, and using

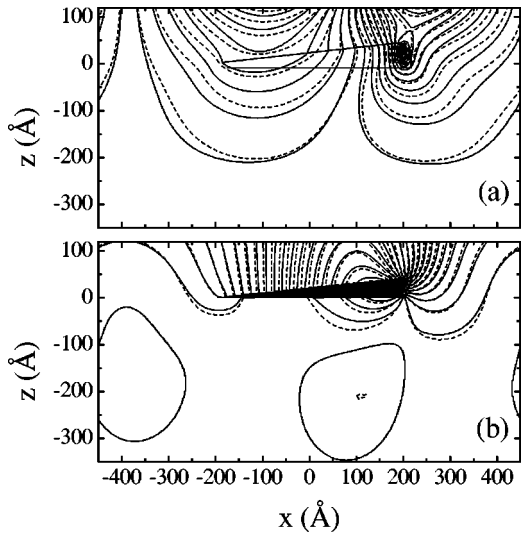

FIG. 7. Comparison of the displacement fields $u_x(x,z)$ [panel (a)] and $u_z(x,z)$ (b) of a single buried wire calculated by FEM (dashed lines) and by our analytical approach (full lines). The step of the contours is $\Delta u = 0.05$ Å.

our approach. The figure shows the displacement fields of a single triangular wire, corresponding to the wire shape in our sample. It is obvious that the analytical and FEM calculations yield nearly identical results. The slight differences may result from the discretization of the grid in the FEM calculations or from the fact that the actual elastic parameters of the wire and the Si matrix are different.

B. Calculation of the scattered intensity

In this section, expressions are derived which describe the distribution of the *diffusely* scattered intensity $I(\mathbf{Q})$ in reciprocal space (the coherent truncation rod scattering is excluded from the calculation). In GID scattering geometry the reduced scattering vector $\mathbf{Q}=\mathbf{K}_f-\mathbf{K}_i-\mathbf{h}$ has to be corrected for refraction and absorption: $\mathbf{q}=\mathbf{k}_f-\mathbf{k}_i-\mathbf{h}$, where $\mathbf{k}_{i,f}$ are the wave vectors of the primary and scattered beams, respectively, corrected for refraction and absorption in the crystal lattice.

The calculation of the scattered intensity is based on the solution of the wave equation

$$(\triangle + K^2)\mathbf{E}(\mathbf{r}) = \hat{\mathbf{V}}\cdot\mathbf{E}(\mathbf{r}), \tag{21}$$

where $\hat{\mathbf{V}} = -K^2\chi(\mathbf{r})$ is the scattering potential and $\chi(\mathbf{r})$ is the crystal polarizability. In a slightly deformed crystal, the polarizability can be expressed as a modified Fourier series

$$\chi(\mathbf{r}) = \sum_{\mathbf{g}} \chi_{\mathbf{g}}(\mathbf{r})\exp[i\mathbf{g}\cdot[\mathbf{r}-\mathbf{u}(\mathbf{r})]],$$

the zero-order Fourier coefficient of the polarizability $\langle\chi(\mathbf{r})\rangle \equiv \chi_0$ is responsible for refraction, its $\mathbf{h}$th coefficient describes the diffraction with the diffraction vector $\mathbf{h}$. The displacement field $\mathbf{u}(\mathbf{r})$ is caused by the buried wire array and the spatial dependence of the Fourier coefficients $\chi_{\mathbf{g}}(\mathbf{r})$ reflects the local changes in the chemical composition. In the following, we restrict to the *S* polarization only. We solve the wave equation by means of the distorted-wave Born approximation, where the scattering potential is divided into two parts $\hat{\mathbf{V}} = \hat{\mathbf{V}}_A + \hat{\mathbf{V}}_B$, where $\hat{\mathbf{V}}_A$ describes an unperturbed system and $\hat{\mathbf{V}}_B$ the perturbation. Here, we choose a semi-infinite Si substrate as the unperturbed system and we solve the wave equation with $\hat{\mathbf{V}}_A = -K^2\chi_{\mathbf{0}}^{\mathrm{Si}}$, i.e., only refraction processes in the substrate ($\chi_{\mathbf{0}}^{\mathrm{Si}}$) are treated dynamically, but diffraction processes with $\mathbf{g}=\mathbf{h}$ included in

$$\hat{\mathbf{V}}_B = -K^2\chi_{\mathbf{h}}(\mathbf{r})\exp[-i\mathbf{h}\cdot\mathbf{u}(\mathbf{r})] \tag{22}$$

are treated kinematically. We choose two independent solutions $E_i^{(A)}(\mathbf{r})$ and $E_f^{(A)}(\mathbf{r})$ of this equation (the latter being time inverted) so that their corresponding incident components in vacuum are the actual primary and scattered beams[32,33]

$$E_i^{(\mathrm{inc})}(\mathbf{r}) = e^{i\mathbf{K}_i\cdot\mathbf{r}}, \quad E_f^{(\mathrm{inc})}(\mathbf{r}) = e^{i\mathbf{K}_f\cdot\mathbf{r}}.$$

In the substrate,

$$E_i^{(A)}(\mathbf{r})\big|_{z<0} = t_i e^{i\mathbf{k}_i\cdot\mathbf{r}}, \quad E_f^{(A)}(\mathbf{r})\big|_{z<0} = t_f^* e^{i\mathbf{k}_f\cdot\mathbf{r}}$$

holds, where $t_{i,f}$ are the Fresnel transmittivities of the surface for the primary and scattered beams, respectively, and $\mathbf{k}_{i,f}$ are the wave vectors corrected to refraction and absorption in the unperturbed system.

The intensity scattered from the wires is proportional to the differential cross section of the scattering due to $\hat{\mathbf{V}}_B$

$$\left(\frac{d\sigma}{d\Omega}\right)_B = \frac{1}{16\pi^2}|\langle E_f^{(A)}|\hat{\mathbf{V}}_B|E_i^{(A)}\rangle|^2. \tag{23}$$

In our model, the SiGe WL's are not included, because these would affect the intensity only at the coherent rod, i.e., around the zeroth lateral satellite.

Assuming a perfect lateral periodicity of the wires, we obtain for the scattered intensity the following expression:

$$I(\mathbf{Q}) = \mathrm{const}\times\delta(Q_y)\sum_P \delta(Q_x-P)|F_P(q_z)|^2. \tag{24}$$

This equation describes an intensity distribution concentrated in periodic satellite peaks forming the one-dimensional reciprocal lattice determined by the lateral wire periodicity (lateral satellites). We have denoted by $F_P(q_z)$ the structure factor of the wire corresponding to the vector P of the one-dimensional reciprocal lattice. Since the wires are elongated along the *y* direction, the strain field and the polarizability do not depend on *y* and the intensity exhibits a sharp peak at $Q_y = 0$. The Pth structure factor is given by (see also Ref. 34)

$$F_P(q_z) = \mathrm{const}\times t_i t_f \int_{-\infty}^{T} dz \int_{-L/2}^{L/2} dx\, e^{-i[Px+q_z(z-T)]} \times[\chi_{\mathbf{h}}(x,z)e^{-i\mathbf{h}\cdot\mathbf{u}(x,z)} - \chi_{\mathbf{h}}^{\mathrm{Si}}], \tag{25}$$

where $\chi_{\mathbf{h}}^{\mathrm{Si}}$ is the hth coefficient of the crystal polarizability of the host lattice and

$$\chi_{\mathbf{h}}(x,z)=(\chi_{\mathbf{h}}^{\mathrm{w}}-\chi_{\mathbf{h}}^{\mathrm{Si}})\Omega(x,z)+\chi_{\mathbf{h}}^{\mathrm{Si}}$$

is the modulated polarizability of the wire array. In Eq. (25) we have excluded the crystal truncation rod from the structure factor by subtracting $\chi_{\mathbf{h}}^{\mathrm{Si}}$ from the local polarizability coefficient $\chi_{\mathbf{h}}(\mathbf{r})\exp[-i\mathbf{h}\cdot\mathbf{u}(\mathbf{r})]$. The phase function $\mathbf{h}\cdot\mathbf{u}(x,z)$ is calculated using Eqs. (16) and (20).

The infinitely sharp δ-like lateral satellite peaks in Eq. (24) are valid for a perfect lateral periodicity of the array of wires. In the experiment, the satellite peaks are broadened due to the finite angular resolution and the deviations from perfect periodicity of the wire positions. While the finite resolution broadens all the satellites by the same amount, a random distribution of the distances of the neighboring wires causes an increase of the satellite widths with increasing $|P|$. Taking both effects into account and neglecting the sharp peak in the Q_y dependence of the intensity, we obtain for the intensity distribution in the Q_xQ_z plane a modified expression

$$I(Q_x,Q_z)=\mathrm{const}\times\sum_P \mathcal{R}_P(Q_x-P)|F_P(q_z)|^2, \quad (26)$$

where the narrow intensity peaks are smeared out by a Lorenzian function

$$\mathcal{R}_P(Q_x)=\frac{1}{\pi\sigma_P}\frac{1}{1+\left(\frac{Q_x}{\sigma_P}\right)^2}, \quad (27)$$

where integrals of these functions were normalized to unity.

Following from the short-range-order model of the wire positions[35,24] the width σ_p of the Pth function depends on the order p of the lateral satellite according to the expression

$$\sigma_p=\sqrt{\sigma_0^2+(p\Delta\sigma)^2}, \quad (28)$$

where σ_0 is the width of the zeroth-order satellite caused by the finite experimental resolution, and $\Delta\sigma=\delta(L)/L$ is the broadening due to a disorder $\delta(L)$ of the lateral wire distances. Note that the disorder of the wire positions does not change the *integrated intensities* of the satellites, which always remain proportional to $|F_P|^2$.

IV. ANALYSIS OF THE WIRE STRUCTURE

In order to compare the measured and simulated intensities quantitatively, we have extracted line scans from the measured GID reciprocal space maps along the lines denoted 1 and 2 in Figs. 4(a,b). The resulting scans are plotted in Fig. 8. Using Eq. (26) we fitted these scans, with the satellite intensities $|F_P|^2$ as free parameters. The good agreement of the fit with the experimental data demonstrates that the short-range-order model for the lateral positions of the wires in Eq. (26) well describes the lateral arrangement of the wires.

From the fits we obtain a mean wire distance of $L=(890\pm20)$ Å and a replication angle $\chi=5\pm1°$, in good agreement with the GISAXS measurements. The width of the zeroth-order satellite, caused by the finite experimental resolution, is $\sigma_0\approx1.5\times10^{-3}$ Å^{-1}, and from the broadening

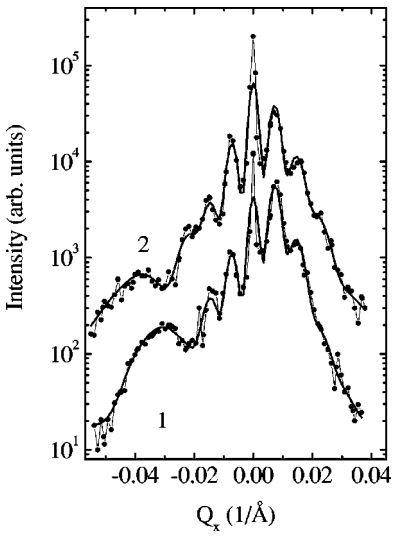

FIG. 8. Line scans extracted from the measured intensity maps along the lines 1 and 2 in Fig. 4(a) (points), together with their fits using Eq. (26) (lines). The scans are shifted vertically for clarity.

of the lateral satellites we obtain a distribution of wire distances with a width of $\delta(L)\approx125$ Å.

The resulting parameters $|F_P|^2$ of the lateral satellites are plotted as full circles in Fig. 9. They have been simulated using the expressions given in Sec. II [Eqs. (16), (20), and (25)]. The wires have a triangular cross section with a base length A of 350 Å and a large side facet inclined by an angle $\beta_1=6°$ with respect to the growth plane. The small-angle scattering data are not sensitive to the slope β_2 of the shorter sidewall of the wire (see Fig. 3). In the simulations we have found that this angle has only negligible influence on the results in the range from $\beta_2=60°$ to $\beta_2=90°$ and we have therefore assumed $\beta_2=90°$ in all simulations. It turns out that a good agreement with the experimental GID data can actually be achieved for various combinations of values for β_1 and x_{Ge}: In GID we are mainly sensitive to the strain variation. Increasing β_1, i.e., increasing the aspect ratio of the wires, will lead to an increase in the in-plane relaxation. However, increasing the Ge content x_{Ge} will have a very similar effect, and hence the two quantities cannot be separated from the GID data alone. Knowing β_1 from our GISAXS experiment, it is possible to determine x_{Ge} by fitting the structure factors $|F_P|^2$ unambiguously. The intensity of the zeroth-order peak has to be excluded from the comparison since it is influenced by the coherent truncation rod and coherent scattering was not taken into account in our simulations. The best correspondence was achieved for $x_{\mathrm{Ge}}=(20\pm10)\%$.

The correspondence of the experimental satellite integrated GID intensities $|F_P|^2$ with the simulated ones is not perfect. The discrepancy could be caused by, e.g., an inhomogeneous distribution of Ge atoms in the volume of the wires. However, it is obvious from this comparison that the mean Ge content in the wires is substantially *lower* than the composition of deposited SiGe alloy with a Ge content of 45%.

The unexpected experimental finding of a Ge content of

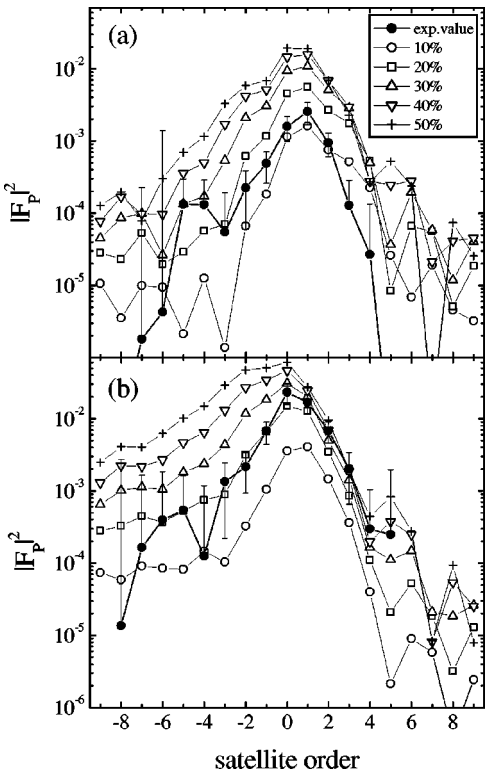

FIG. 9. Integrated satellite intensities $|F_P|^2$ of the lateral satellites obtained from the linear scans in Fig. 8 (black circles), and their simulations for various Ge concentrations x_{Ge} in the wires. The panels (a) and (b) show the experimental satellite intensities in the scans 1 and 2 in Fig. 8, respectively, along with the corresponding simulated values. The abscissa position of data points corresponds to the order of the lateral satellites.

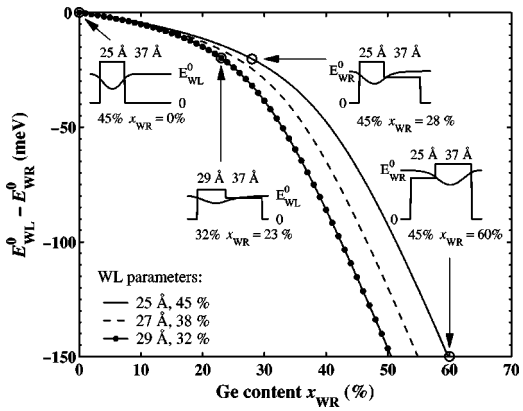

FIG. 10. Calculated difference between the ground-state energies of heavy holes confined to the wetting layer (E^0_{WL}) and to the quantum wire (E^0_{WR}) as a function of the Ge content x_{WR} of the wire (thickness: 37 Å) assembled on top of the wetting layer. E^0_{WL}-E^0_{WR} is plotted for the three different wetting layer compositions indicated in the plot. As discussed in the text, in the calculation, the quantum wires are modeled by step quantum wells. The alignment of the heavy-hole valence-band edge in growth direction, the ground-state wave functions, and energies are sketched in the insets for a 25 Å, 45% wetting layer (the Ge content in the wire is $x=0\%$) and for three step quantum wells modeling the wire structure. For $E^0_{WL}-E^0_{WR}=-20$ meV (corresponding to the energy difference of the NP_{WL} and NP_{WR} lines observed in the PL spectra of samples *C*), the heavy-hole band alignments are shown in the insets for two wetting layer compositions: the nominal for sample *C* and the one determined by the HRXRD experiments, respectively. In the plot, the points corresponding to structures shown in the insets are marked by ○.

the self-organized wires lower than that in the WL is also reflected in the PL spectra of samples *B* and *C* containing wires: Figure 5 shows that the quantum-wire no-phonon line (NP_{WR}) is shifted to a lower energy with respect to the NP_{WL} line in the spectra of samples *B* and *C* by an amount as small as ≈ 20 meV. In order to correlate the observed small shift with the Ge concentration in the quantum wires, we have calculated the confinement energies in the WL and in the quantum wires. Since the extension of the wires in the lateral direction is approximately ten times larger than in the vertical direction, in the calculations we neglect the lateral confinement and model the quantum wire structure by a step quantum well consisting of the WL and the self-assembled wire part. Figure 10 shows the difference between the calculated ground-state energies E^0_{WL} of the the wetting layer alone and E^0_{WR} of the step quantum well (modeling the quantum wire) as a function of the Ge content within the self-organized wires. This difference models the energy shift between the no-phonon lines for the quantum well and wire, observed in the PL spectra (Fig. 5) of samples *B* and *C*. The calculations using the $k\cdot p$ model[36] have been performed for three different compositions of the WL: the nominal composition for sample *C* (25 Å,45%), a composition close to the composition of sample *C* determined by x-ray diffraction (29 Å,32%) and for a composition between these two compositions (27 Å,38%). The insets of Fig. 10 show the valence-band alignment for heavy holes together with the square moduli of the ground-state wave function for several selected parameter combinations. Obviously the small difference of 20 meV between the energies of the no-phonon lines of wire and well can be explained within this model only if a germanium concentration between 20% and 30% is assumed in the self-assembled part of the wire (for all three parameter pairs assumed for the WL composition). Therefore, the results of the PL measurements are in excellent agreement with the results obtained by GID experiments, confirming that the Ge content in the wires is indeed *lower* than that of the deposited alloy, in contrast to the behavior of buried self-assembled SiGe islands, which usually have a Ge content higher than the WL.[37]

V. SUMMARY

Self-organized *buried* SiGe wires in a 20-period SiGe/Si multilayer sample with 45% deposited germanium content were investigated by grazing-incidence x-ray diffraction. The laterally periodic wires in the Si/SiGe superlattice, which is grown on a vicinal (001) Si substrate with a miscut angle of about 3.5°, are oriented along the [010] direction. An analytical model for the strain fields within the SiGe wires and in the Si matrix was derived. The inhomogeneous strain

fields resulting from this model serve as an input for the simulation of the scattered intensities in GID geometry, using distorted-wave Born approximation. Using the shape of the wires obtained by GISAXS experiments, the simulations of the GID intensity distribution yield an average Ge content of 20%, lower than in the wetting layers. Most likely, this decrease of the Ge content in the wires is caused by a diffusion process during overgrowth. The behavior, which is confirmed by photoluminescence experiments, is different from self-organized islands, which usually contain more Ge than the underlying wetting layers. In order to account for these results, growth models for self-organized wires which include diffusion during overgrowth will have to be developed.

The presented strain analysis is applicable to all self-organized as well as etched and buried nanostructures with planar surfaces.

ACKNOWLEDGMENTS

We thank J.-H. Zhu, K. Brunner, and G. Abstreiter, Walter-Schottky Institut, Technische Universität in München, Germany for providing SiGe wire samples. This work was supported by FWF Austria (Project No. P-11557), EC project SiGeNET (HPRN-CT-1999-00123), and by the Grant Agency of Czech Republic (Project No. 202/00/0354). Synchrotron experiments were carried out at the TROIKA II beamline of the ESRF, Grenoble, France. We acknowledge the valuable help of O. Konovalov (ESRF) with the beamline setup.

*Permanent address: Laboratory of Thin Films and Nanostructures, Institute of Condensed Matter Physics, Masaryk University, Kotlářská 2, 611 37 Brono, Czech Republic.

[1] C. Schelling, M. Mühlberger, G. Springholz, and F. Schäffler, Phys. Rev. B **64**, 041302(R) (2001).
[2] C. Teichert, J.C. Bean, and M.G. Lagally, Appl. Phys. A: Mater. Sci. Process. **67**, 675 (1998).
[3] G.M. Ribeiro, A.M. Bratkovsky, T.I. Kamins, D.A.A. Ohlberg, and R.S. Williams, Science **279**, 353 (1998).
[4] A. Rastelli, M. Kummer, and H. von Känel, Phys. Rev. Lett. **87**, 256101 (2001).
[5] C.P. Liu, J.M. Gibson, D.G. Cahgill, T.I. Kamins, D.P. Basile, and R.S. Wiliams, Phys. Rev. Lett. **84**, 1958 (2000).
[6] C. Giannini, T. Baumbach, D. Lübbert, R. Felici, L. Tapfer, T. Marschner, W. Stolz, N.Y. Jin-Phillipp, and F. Phillipp, Phys. Rev. B **61**, 2173 (2000).
[7] N. Liu, J. Tersoff, O. Baklenov, A.L. Holmes, Jr., and C.K. Shih, Phys. Rev. Lett. **84**, 334 (2000).
[8] J. Stangl, T. Roch, V. Holý, M. Pinczolits, G. Springholz, G. Bauer, I. Kegel, T.H. Metzger, J. Zhu, K. Brunner, G. Abstreiter, and D. Smielgies, J. Vac. Sci. Technol. B **18**, 2187 (2000).
[9] V. Holý, A. Darhuber, J. Stangl, S. Zerlauth, F. Schäffler, G. Bauer, N. Darowski, D. Lübbert, U. Pietsch, and I. Vávra, Phys. Rev. B **58**, 7934 (1998).
[10] J. Stangl, V. Holý, T. Roch, A. Daniel, G. Bauer, Y.H. Zhu, K. Brunner, and G. Abstreiter, Phys. Rev. B, **62**, 7229 (2000).
[11] J. Tersoff and R.M. Tromp, Phys. Rev. Lett. **70**, 2782 (1993).
[12] W. Ma, R. Nötzel, A. Trampert, M. Ramsteiner, H. Zhu, H.P. Schönherr, and K.H. Ploog, Appl. Phys. Lett. **78**, 1297 (2000).
[13] L. Vescan, Thin Solid Films **294**, 284 (1997).
[14] K. Brunner, J. Zhu, C. Miesner, G. Abstreiter, O. Kienzle, and F. Ernst, Physica E (Amsterdam) **7**, 881 (2000).
[15] A.A. Darhuber, J. Zhu, V. Holý, J. Stangl, P. Mikulík, K. Brunner, G. Abstreiter, and G. Bauer, Appl. Phys. Lett. **73**, 1535 (1998).
[16] F. Liu, J. Tersoff, and M.G. Lagally, Phys. Rev. Lett. **80**, 1268 (1998).
[17] C. Schelling, G. Springholz, and F. Schäffler, Phys. Rev. Lett. **83**, 995 (1999).
[18] C. Schelling, G. Springholz, and F. Schäffler, Thin Solid Films **380**, 20 (2000).
[19] J. Zhu, K. Brunner, and G. Abstreiter, Appl. Phys. Lett. **73**, 620 (1998).
[20] J. Zhu, K. Brunner, G. Abstreiter, O. Kienzle, F. Ernst, and M. Rühle, Phys. Rev. B **60**, 10 935 (1999).
[21] T. Baumbach, D. Lübbert, and M. Gailhanou, J. Appl. Phys. **87**, 3744 (2000).
[22] Th. Wiebach, M. Schmidbauer, M. Hanke, H. Raidt, R. Köhler, and H. Wawra, Phys. Rev. B **61**, 5571 (2000).
[23] I. Kegel, T.H. Metzger, P. Fratzl, J. Peisl, A. Lorke, J.M. Garcia, and P.M. Petroff, Europhys. Lett. **45**, 222 (1999).
[24] V. Holý, T. Roch, J. Stangl, A. Daniel, G. Bauer, T.H. Metzger, Y.H. Zhu, K. Brunner, and G. Abstreiter, Phys. Rev. B **63**, 205318 (2001).
[25] J. Zhu, K. Brunner, and G. Abstreiter, Appl. Phys. Lett. **72**, 424 (1998).
[26] M. Wachter, F. Schäffler, H.J. Herzog, K. Thonke, and R. Sauer, Appl. Phys. Lett. **63**, 376 (1993).
[27] J. Weber and M.I. Alonso, Phys. Rev. B **40**, 5683 (1989).
[28] V. Holý, A.A. Darhuber, J. Stangl, G. Bauer, J. Nützel, and G. Abstreiter, Semicond. Sci. Technol. **13**, 590 (1998).
[29] Y. Yoneda, Phys. Rev. **131**, 2010 (1963).
[30] V. M. Kaganer, B. Jenichen, G. Paris, K.H. Ploog, O. Konovalov, P. Mikulík, and S. Arai (unpublished).
[31] S.P. Timoschenko, *Theory of Elasticity* (McGraw-Hill, New York, 1961); J.P. Hirth and J. Lothe, *Theory of Dislocations* (McGraw-Hill, New York, 1968).
[32] V. Holý, U. Pietsch, and T. Baumbach, *High Resolution X-Ray Scattering from Thin Films and Multilayers* (Springer, Berlin, 1999).
[33] S.K. Sinha, E.B. Sirota, S. Garoff, and H.B. Stanley, Phys. Rev. B **38**, 2297 (1988).
[34] M.A. Krivoglaz, *Diffuse Scattering of X-Rays and Neutrons by Fluctuations* (Springer, Berlin, 1996).
[35] I. Kegel, T.H. Metzger, J. Peisl, P. Schittenhelm, and G. Abstreiter, Appl. Phys. Lett. **74**, 2978 (1999); I. Kegel, T.H. Metzger, J. Peisl, J. Stangl, G. Bauer, and D. Smilgies, Phys. Rev. B **60**, 2516 (1999).
[36] T. Fromherz, E. Koppensteiner, M. Helm, G. Bauer, J.F. Nützel, and G. Abstreiter, Phys. Rev. B **50**, 15 073 (1994).
[37] P. Venezuela, J. Tersoff, J.A. Floro, E. Chason, D.M. Follstaedt, Feng Liu, and M.G. Lagally, Nature (London) **397**, 678 (1999).